Langmuir

Article

pubs.acs.org/Langmuir

Monte Carlo Simulation of Cavitation in Pores with Nonwetting Defects

Christopher J. Rasmussen, Gennady Yu. Gor,† and Alexander V. Neimark*

Rutgers, The State University of New Jersey, Department of Chemical and Biochemical Engineering, 98 Brett Road, Piscataway, New Jersey, 08854, United States

ABSTRACT: We investigate the onset of cavitation in a metastable fluid confined to nanoscale pores with nonwetting defects present. Using grand canonical and gauge cell mesocanonical Monte Carlo simulations, we study the degree of metastability (relative vapor pressure), at which the critical bubble forms in a spherical pore with a circular nonwetting defect. It is shown that an increase of the defect size leads to a transition from homogeneous to heterogeneous nucleation of critical bubbles formed at the defect site. In this case, the desorption process may be initiated at larger relative vapor pressures than those predicted by the theories of homogeneous cavitation.

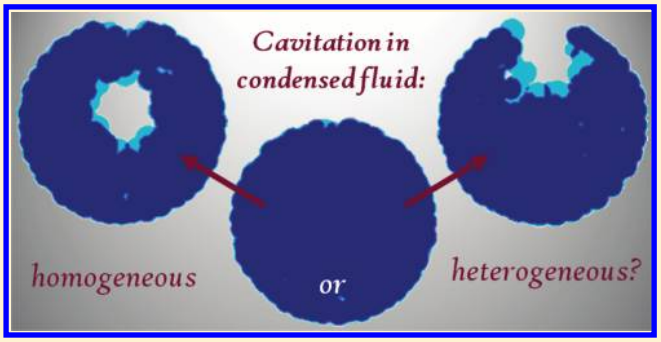

1. INTRODUCTION

The role of cavitation during the evaporation of a fluid from porous materials has been a much-discussed topic.[1−9] When the formation of an equilibrium meniscus at the vapor−liquid interface is somehow hindered, desorption occurs at a pressure less than the vapor−liquid equilibrium (VLE) pressure for the pore of a given size. In particular, there is much interest in so-called "ink-bottle" mesopores, where a pore body is connected to other pores by smaller channels or necks. As known from the experiments and respective theories, the neck diameter has a profound effect on the position of the evaporation pressure.[5] The smaller is the neck diameter, the smaller is the relative pressure of desorption p_{des}/p_0, (p_0 is the vapor pressure of the bulk). This is referred to as the pore blocking regime of desorption. However, below a certain critical neck diameter, which is about 4−5 nm in the case of nitrogen adsorption at 77.4 K, the experimental relative desorption pressure no longer depends on the neck size and varies in a narrow interval ($p_{des}/p_0 = 0.47 \pm 0.03$).[4] This regime of desorption is related to the cavitation of metastable fluid in the pore body. As the external vapor pressure is lowered, the fluid in the pore body becomes overstretched (metastable), and eventually, unstable. As the limit of fluid stability is approached (near the spinodal point), a critically sized bubble nucleus forms, which grows rapidly causing spontaneous desorption of the fluid from the pore body, despite the pore neck remaining filled.

Although the importance of the cavitation phenomenon in the process of capillary evaporation was well understood,[10−13] only during the past decade has it been studied extensively, both experimentally[1,2,4−6,9,14−18] and with computer simulation.[3,4,8,19−25] Sarkisov and Monson first implemented grand canonical molecular dynamics in a slit-shaped pore geometry and observed emptying of the main pore body while the connecting necks remained filled.[24,25] Quantitative experimental studies of cavitation[5] became possible with the advent of highly ordered, templated mesoporous silicas.[26] These are designer materials with a narrow, uniform distribution of pore sizes that can be tailored to desired sizes.[17] These materials provide an opportunity for direct comparison of the results of theoretical and simulation approaches to experimental data. A comprehensive study of cavitation in ordered 3D cage-like structures of SBA-16 and FDU-1 materials was performed by Ravikovich and Neimark,[5] who combined the adsorption measurements with nonlocal density functional theory (DFT) calculations to determine the pore dimensions. They found that the transition from the cavitation regime of desorption to the pore blocking regime occurs not only with the increase of the pore neck size, but also with a temperature decrease for a given pore geometry. With similar methods, Thommes et al.[6] explored cavitation on mesoporous silicas of hierarchical structure. Morishige et al.[9] also observed desorption pressures near $p/p_0 = 0.47$ for nitrogen in silica ink-bottle pores, and found that increasing temperatures allows for cavitation in pores with larger connecting necks. Vishnyakov and Neimark[20] studied the transition from pore blocking to cavitation with a decrease of the neck size using Monte Carlo (MC) simulations. Libby and Monson[23] modeled desorption from ink-bottle pores with lattice DFT and MC and confirmed that the transition from the pore blocking to cavitation regimes depends on the pore geometry and temperature. Rasmussen et al.[4] studied the effect of the pore body size on the onset of cavitation. On the basis of MC simulations performed for a variety of experimentally studied systems, they found that the cavitation pressure increases with the increase of the pore body size from

Received: January 5, 2012
Revised: February 10, 2012
Published: February 13, 2012

7 to 10 nm, but in a very narrow range of relative pressures from ∼0.45 to ∼0.5. In pores larger than ∼10 nm the cavitation pressure did not depend on the pore size and the cavitation occurs similarly to that in the bulk fluid. As such, it was concluded that the cavitation of nitrogen at its boiling temperature cannot occur at $p/p_0 > 0.50-0.52$. More recent molecular simulation studies of cavitation,[3,8,23,27] as well as multiple experimental studies,[1,6,15,16,18] confirm the main features of this phenomenon described above.

The current work has been triggered by a discussion in the literature about the mechanism of desorption of fluids confined to porous silicon (PSi), a material with nonintersecting hexagonally ordered unidirectional pore channels. In PSi samples prepared and studied by different groups, a sharp desorption step is observed at relative pressures significantly larger that the range of cavitation pressures in other mesoporous materials, e.g., at $p_{des}/p_0 > 0.6-0.7$, for the case of nitrogen.[2,28−30] At the same time, this pressure is smaller than the equilibrium vapor pressure characteristic for the pore channels of given size that would be expected of the desorption pressure in open-ended cylindrical channels.[31] Moreover, with experiments performed with specially designed, deposited, and layered PSi samples, the authors of refs 2, 29, and 30, did not find sizable variations of the desorption pressure in the open-ended channels, channels closed at the bottom, and ink-bottled channels thus posing a question about the validity of the basic concepts of the mechanisms of capillary condensation hysteresis accepted in the literature.[32,33] One explanation for these phenomena is a corrugation of pore channels leading to pore blocking effects.[29] This was confirmed by computational studies by modeling linear pores with mesoscopic roughness.[28,34] In addition, chemical smoothing of PSi channels appears to shift the desorption mechanism toward near-equilibrium desorption, suggesting roughness is responsible for characteristic desorption pressure.[35] However, Grosman and Ortega,[2] as well as Naumov et al.,[28,34] suggested that desorption in PSi channels may exhibit cavitation. The main obstacle for accepting cavitation as the *primary* mechanism of desorption in PSi is the conclusion derived in our previous paper[4] that the cavitation cannot occur at such large relative pressures. However, this conclusion entails that the pore walls are wetting, and as such, the cavitation occurs in a homogeneous fashion, with the critical bubble more likely formed at the pore center rather than at the solid surface. To support the cavitation hypothesis, Grosman and Ortega[2] suggested that the cavitation of metastable nitrogen in PSi channels occurs at some heterogeneities on the pore walls, and it is a heterogeneous, rather than homogeneous, process, which due to smaller nucleation barriers may take place at respectively larger vapor pressures.

In this work, as a continuation of our previous studies of homogeneous cavitation,[4] we evaluated the influence of a heterogeneity of the pore wall on the vapor pressure at which cavitation occurs. We considered the heterogeneous defects on the pore wall as nonwetting spots of molecular size. We applied two approaches for quantitative estimates, the macroscopic classical nucleation theory (CNT) and detailed MC simulation in grand canonical (GCMC) and mesocanonical (MCMC) ensembles. As an instructive example, we model the behavior of a Lennard−Jones (LJ) fluid in a spherical pore with wetting LJ walls, which contained a single circular nonwetting defect. To provide quantitative relevance to experimental studies and earlier simulations, the potential parameters for the LJ model of nitrogen adsorption on silica at nitrogen's normal boiling temperature of 77.36 K employed in previous work were used here.[36,37] We found that as the size of the nonwetting defect increases, the mechanism of cavitation changes from homogeneous to heterogeneous. Since it is doubtful that defects, which would be nonwetting to condensed nitrogen, exist in PSi, the results of this work cannot be immediately applied to the PSi desorption pressure enigma discussed above. However, the phenomenon of heterogeneous cavitation cannot be ruled out for other systems with polar fluids, such as water.

2. HETEROGENEOUS VS HOMOGENEOUS—CLASSICAL NUCLEATION THEORY APPROACH

Cavitation is necessarily preceded by the formation of a critically sized bubble, or nucleus. Bubbles smaller than the critical size collapse back into the fluid state. Once a critically sized bubble nucleates, thermal fluctuations can increase the bubble's size to a point where it grows irreversibly and displaces the adsorbed fluid; this is desorption by cavitation. CNT[38,39] describes the thermodynamics of formation of a nucleus in the bulk system. Since CNT operates with macroscopic values, it cannot give reliable quantitative predictions when applied in the nanoscale.[40] However, CNT allows one to obtain a transparent qualitative description of the nucleation phenomenon. We use CNT to estimate the work of bubble formation for two different nucleation events: homogeneous nucleation—when the bubble forms in presumably uniform fluid inside the pore and thus does not depend on the pore size and surface chemistry, and heterogeneous nucleation—when the bubble nucleates on the pore wall and does depend on the surface defects.

According to CNT, the work of homogeneous nucleation of a critical vapor bubble of spherical shape is determined by the Gibbs equation, as the difference between the work of surface formation and the work of compression,

$$W_{\mathrm{homo}}(r_{\mathrm{b}}) = 4\pi r_{\mathrm{b}}^2\gamma - \frac{4}{3}\pi r_{\mathrm{b}}^3\Delta p \tag{1}$$

where γ is the liquid−vapor surface tension, and r_{b} is the radius of critical bubble, and Δp is the capillary pressure, or the pressure difference between the vapor inside the bubble and the liquid outside the bubble:

$$\Delta p = p_{\mathrm{l}} - p_{\mathrm{v}} = \frac{2\gamma}{r_{\mathrm{b}}} \tag{2}$$

where p_{v} and p_{l} are the pressures of equilibrium liquid and vapor phases determined for a given chemical potential through a bulk equation of state. A standard assumption of ideal vapor and incompressible liquid is usually used to relate the capillary pressure and, respectively, the radius of the critical bubble, to the relative vapor pressure, p/p_0, through the Kelvin-Laplace equation:

$$\frac{2\gamma}{r_{\mathrm{b}}} = -\frac{R_{\mathrm{G}}T}{V_{\mathrm{m}}}\ln\frac{p}{p_0} \tag{3}$$

where R_{G} is the gas constant and V_{m} is the molar volume of the liquid adsorbate. In our previous work, we found that eq 1 correctly predicts the asymptotic value of the nucleation barrier calculated by MC simulation for a LJ fluid confined to spherical nanopores as the pore size increases, but it becomes progressively inaccurate for pores smaller that 10 nm.[4]

dx.doi.org/10.1021/la300078k | Langmuir 2012, 28, 4702−4711

For the convenience of dimensionless analysis, all scales can be reduced to the fluid molecular diameter σ, and eq 3 can be rewritten as follows:

$$\frac{r_b}{\sigma} = -\frac{\chi_c}{\ln(p/p_0)} \quad (4)$$

where $\chi_c = 2\gamma V_m/R_G T$ is the dimensionless parameter that relates the theoretical nucleus size, $a_c = 2\gamma\sigma V_m/R_G T$, at a characteristic pressure $p/p_0 = 1/e = 0.37$, to the molecular diameter σ. For nitrogen at its normal boiling temperature $T = 77.4$ K (the experimental standard in adsorption measurements), $\sigma = 0.36$ nm, $a_c = 0.96$ nm, and $\chi_c = 2.7$. These numbers give the reader the characteristic scale of the phenomenon we are concern with. It is worth noting that we use the bulk values of surface tension γ without Tolman-type corrections[41] for the bubble's curvature; this simple model is sufficient for demonstration of qualitative mechanisms of cavitation.

To investigate heterogeneous bubble nucleation, we consider a spherical pore of radius R with a nonwetting defect of radius r_{def}. The bubble must be pinned to the defect perimeter, which represents the three phase contact line, see schematics in Figure 1,

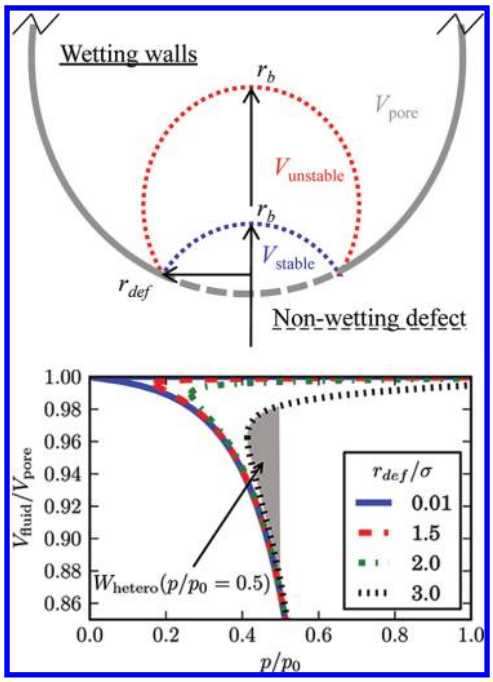

Figure 1. Top: Schematics of heterogeneous bubble growth at the circular nonwetting defect in the spherical pore. The bubble is pinned to the defect; equilibrium conditions permit two solutions, the smaller *stable* bubble, and the larger *unstable* bubble. Note that the radius r_b is identical for these two configurations and it is determined by eq 2. Bottom: Isotherms calculated using eq 4 and the appropriate bubble volume (see ref 42), displayed as the fraction of pore volume filled by liquid condensate versus the relative pressure. The ascending, upper branch corresponds to the stable bubble, and the descending, lower branch to the unstable bubble. The branches meet at a spinodal-type point where their respective bubbles' volumes are equal and the work of formation vanishes; at this point $r_b = r_{def}$ and the bubble is hemispherical. The work of formation of an unstable bubble is related to the area between the two branches at a given pressure.

top. Note that because in this case the contact line cannot move, the concept of the contact angle in not applicable. The bubble pinned to the defect boundary exists even at the saturation conditions, $p/p_0 = 1$, when the bubble interface is flat (e.g., $r_b \to \infty$) and the bubble forms a spherical cap. Upon desorption, as the relative pressure decreases, the equilibrium bubble grows maintaining a spherical vapor–liquid interface of radius r_b, which decreases with pressure according to eq 3. The pinned bubble is bound by two coinciding spherical caps of radii R and r_b; its volume can be found through simple geometrical relationships, see ref 42. It is important to note that at a given relative pressure there are two equilibrium configurations, small and large, for the bubble of given size r_b, provided the bubble radius r_b is larger than the defect radius r_{def} and smaller than the pore radius R, $r_{def} < r_b < R$. It is easily seen that the small bubble is stable against variations of its volume at given vapor pressure, and large bubble is unstable. In other words, the unstable large bubble represents the critical nucleus that should be formed due to thermal fluctuations.

In the bottom of Figure 1, we present the desorption isotherm that corresponds to the growing bubble pinned at the defect, calculated according to the Kelvin-Laplace equation (eq 3). It represents the normalized fraction of the pore volume filled by condensed fluid (i.e., the relative fluid volume outside the bubble, $[(4/3)\pi R^3 - V(r_b)]/[(4/3)\pi R^3]$). This isotherm has two branches: the upper branch is that of the stable bubbles with the radius varying from R at $p/p_0 = \exp(-a_c/R)$ to r_{def} at $p/p_0 = \exp(-a_c/r_{def})$. Note that for clarity the isotherms were continued to $p/p_0 = 1$, corresponding to the flat liquid–vapor interface. In this case, the radius of the stable bubble exceeds the radius of the pore, $r_b > R$. The lower backward branch is that of the unstable bubble, or critical nuclei, with the radius varying from r_{def} to R. The leftmost turnover point corresponds to the spinodal, at which the stable and unstable bubble configurations merge; the radius of such spinodal bubble equals to the radius of the defect, $r_b = r_{def}$. Calculations in Figure 1 were performed for the pore of $R = 7.36$ σ, to correspond with MC calculations presented below, and with defects of several sizes. As the defect size increases, the spinodal point moves toward larger vapor pressures.

Nucleation of the critical bubble is a fluctuation–driven event. The probability to form a critical bubble depends on the work of its formation from the stable bubble at given vapor pressure, or the nucleation barrier that is determined by the work of surface formation and the work of compression. Thus, the nucleation barrier of heterogeneous cavitation is determined by the differences of surface areas and volumes of unstable and stable bubbles by the analog to eq 1, as follows:

$$W_{hetero}(r_b, r_{def}) = \gamma(S_u - S_s) - \frac{2\gamma}{r_b}(V_u - V_s) \quad (5)$$

where the subscript s, u refers to the stable or unstable bubble of given radius r_b. The equations for S_u, S_s, V_u, and V_s are given in ref 42. At the spinodal ($r_b = r_{def}$), the nucleation barrier vanishes. At $r_b > r_{def}$, the nucleation barrier can be calculated by integrating the adsorption isotherm between stable and unstable states along the chemical potential, as indicated by the shaded area in Figure 1, bottom.

Either heterogeneous or homogeneous nucleation in condensed fluid is possible at given external conditions. It is obvious that the energy barrier of heterogeneous nucleation is always smaller than that of homogeneous nucleation, $W_{hetero}(p/p_0) < W_{homo}(p/p_0)$. However, to compare the relative probabilities of homogeneous and heterogeneous nucleation, one has to take into account not only the difference in nucleation barriers but also the volume factor, which increases the probability of homogeneous nucleation. To trigger heterogeneous cavitation, the critical bubble may nucleate only at the site of the defect. To trigger homogeneous cavitation, the critical bubble has the whole volume of liquid as potential nucleation "sites". Assuming that

dx.doi.org/10.1021/la300078k | *Langmuir* 2012, 28, 4702–4711

the homogeneous critical nucleus of radius r_b can be formed with its center located within the spherical core of the pore of radius $R - r_b$, the volume factor can be estimated as the ideal term in the nucleus free energy,

$$F_{id}(r_b) = -k_B T \ln\left[\frac{\frac{4}{3}\pi(R - r_b)^3}{\Lambda^3}\right] \quad (6)$$

where k_B is the Boltzmann constant and Λ is the de Broglie length of a fluid molecule. As such, the ratio of probabilities of a homogeneous nucleation event as opposed to a heterogeneous one at given external conditions can be evaluated as follows:

$$\frac{P_{homo}(r_b)}{P_{hetero}(r_b, r_{def})} = \frac{\frac{4}{3}\pi(R - r_b)^3}{\Lambda^3}\exp\left[-\frac{W_{homo}(r_b) - W_{hetero}(r_b, r_{def})}{k_B T}\right] \quad (7)$$

where W_{homo} and W_{hetero} are determined by eqs 1 and 5, respectively, for a given r_b. The prefactor reflects the entropic contribution given by eq 6. This term can be thought of as the number of potential microscopic nucleation sites in the volume of condensed fluid. Equation 7 predicts a transition from homogeneous cavitation to heterogeneous cavitation as the diameter of the defect grows, and is illustrated in Figure 2.

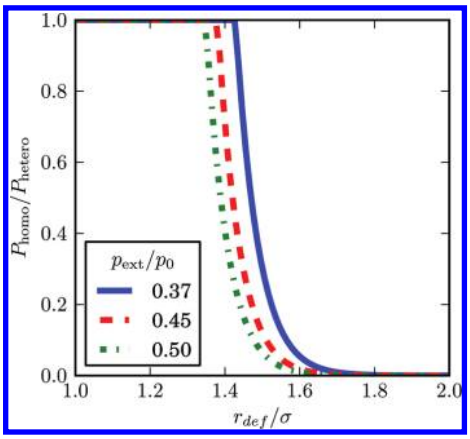

Figure 2. The CNT ratio of probabilities of homogeneous and heterogeneous nucleation as a function of the defect size for a spherical pore $R/\sigma = 7.36$, at several characteristic pressures. Small defects do not influence nucleation. Defects larger than $r_{def}/\sigma \approx 1.5$ present a large enough free energy benefit for heterogeneous nucleation to overcome the entropic advantage of homogeneous nucleation.

The ratio of nucleation probabilities was calculated at various defect sizes for the pore $R = 7.36\ \sigma$, at several typical external pressures. The transition from homogeneous nucleation to heterogeneous nucleation is observed when the diameter of the defect is about $3\ \sigma$. It is important to remember that although the predictions of CNT are qualitatively correct, they cannot be taken as quantitative estimates due to the macroscopic nature of CNT. A more precise description can be achieved by using MC simulation of the adsorption−desorption process that is described below.

3. MC MODEL AND SIMULATION DETAILS

Monte Carlo simulations were used to model cavitation of Lennard−Jones (LJ) fluid in a spherical pore. The pore wall interacts with the adsorbate particles via a continuous, site-averaged LJ potential. We tested a pore with external diameter (distance between the centers of two opposing LJ solid particles) $d_{ext} = 2R = 5.72$ nm $= 15.82\ \sigma$ and accessible diameter (diameter of the volume in which $U_{adsorption} > 0$)[43] $d_{acc} = 5.54$ nm $= 14.72\ \sigma$. The size of the defect, in diameter, was varied from 0 to 2.21 nm ($6.12\ \sigma$). The calculations were done for the LJ model of nitrogen with fluid−fluid interaction parameters of $\varepsilon_{FF}/k_B = 101.5$ K and $\sigma_{FF} = \sigma = 0.36154$ nm.[44] The potential energy was truncated when interparticle distance was greater than $10\ \sigma$. The solid−fluid LJ potential was calculated by integral average over the pore wall surface.[45,46] The solid−fluid interaction parameters were selected to emulate adsorption of nitrogen on silica glass (energy parameter $\varepsilon_{SF}/k_B = 147.3$ K, size parameter $\sigma_{SF} = 0.317$ nm and surface density of adsorption sites $\rho_S = 15.3$ nm^{-2}).[36] For all simulations, temperature was set to the normal boiling point of liquid nitrogen, $T = 77.36$ K. The Johnson−Zollweg−Gubbins (JZG) equation of state for LJ fluids was used to relate the chemical potential to the relative vapor pressure.[47]

A nonwetting defect of variable size was introduced as a round spot on the pore wall which does not exert the attractive potential. Utilizing the cylindrical symmetry of the system, the adsorption potential inside the pore at a point characterized by the distance from the pore center r and the polar angle θ can be expressed as the integral over the sphere surface excluding the surface of spherical cap occupied by the defect,

$$U_{SF}(r, \theta, \delta, R) = 4\varepsilon_{SF}\rho_S R^2 \int_0^{2\pi}\int_\delta^\pi \left(\frac{\sigma_{SF}^{12}}{\xi^{12}} - \frac{\sigma_{SF}^{6}}{\xi^6}\right) \times \sin\theta_0 d\theta_0 d\varphi_0 \quad (8)$$

where r and θ are radius and inclination of a point within the sphere, 2δ is the apex angle of the defect, and subscript "0" indicates integration variables over the spherical surface. Figure 3 illustrates the geometry of the pore/defect system. The distance from a point within the sphere (e.g., an adsorbate molecule) and on the sphere (e.g., an adsorption site) is given by the following:

$$\xi^2 = R^2 + r^2 - 2Rr[\sin\theta\sin\theta_0\cos(\varphi_0 - \varphi) + \cos\theta\cos\theta_0] \quad (9)$$

By performing the integration in θ_0 from δ to π, rather than 0 to π, a conical volume is introduced with no contribution to the potential. A potential energy map of the xz plane of a system with a relatively large defect is presented in Figure 3. A simple trigonometric equation relates δ to the radius of the defect,

$$r_{def} = R\sin\delta \quad (10)$$

The value r_{def} in eq 10 specifies the external, center to center radius of a spherical defect on the pore wall. The accessible diameter of the defect can be estimated by subtracting σ_{SF}/σ_{FF} from $d_{def} = 2r_{def}$. For convenience, all diameters herein will refer to the accessible volume. Increasing the defect diameter reduces the total adsorption potential, which affects the condensation and desorption pressures.[4] However, because the defect is nonwetting, its surface will always be a more favorable nucleation site; thus its area rather than the relative difference in adsorption potential is the primary variable with which we are concerned.

The adsorption potential (eq 8) is a continuous function of two position variables, r and θ. It was integrated numerically and tabulated on a grid of 2000 × 500, respectively. The spherical-linear interpolation method[48] was used to calculate

dx.doi.org/10.1021/la300078k | Langmuir 2012, 28, 4702−4711

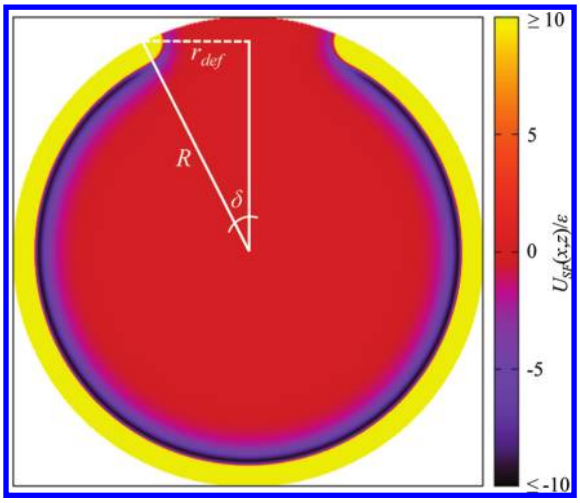

Figure 3. The solid–fluid potential energy map on the *xz*-plane of a 5.54 nm pore with a 2.21 nm nonwetting defect introduced. Overlay: geometry of eqs 8 and 10.

the potential energy from the tabulated values. Boundary conditions at the nonwetting defect were set as hard-wall repulsion. In general, it is possible to extend this model to a partial wetting defect by adding the integrated LJ potential of the conical defect, but with a value of solid–fluid interaction potential smaller than ϵ_{SF}.

Monte Carlo simulations were performed using the grand canonical ensemble (GCMC)[49] and the mesocanonical ensemble (MCMC).[50,51] The MCMC method, also known as the gauge cell method, introduces a fixed reservoir of particles (called the gauge cell) that are permitted to be exchanged with the system cell (the pore). The MCMC method is instrumental in calculating chemical potentials in small and inhomogeneous system.[51] It has been extended since its original formulation[50] to multicomponent fluids[52] and polymer chains.[53,54] The MCMC method allows one to efficiently simulate nucleation phenomena and generate unstable, intermediate states by suppressing fluctuations that would, if unconstrained, facilitate a spontaneous phase change in an open system. As such, MCMC makes possible a continuous, backward trajectory of the adsorption isotherm that corresponds to the unstable bubbles, or nuclei, qualitatively similar to the theoretical isotherm shown in Figure 1. Once such a continuous canonical isotherm is generated, the nucleation barrier at given vapor pressure can be calculated as the work of formation of the unstable bubble from the stable one by thermodynamic integration.[4,19,55,56]

GCMC was used to emulate experimental adsorption conditions of constant chemical potential, volume, and temperature. Because nucleation of the critical bubble is a fluctuation-driven process, the cavitation events are distributed over a certain range of pressures. To obtain this distribution, a number of sequential GCMC desorption trajectories were performed in the following manner:

(1) A true random seed[57] is used to build a random, independent configuration of particles at a given stable liquid density.
(2) The configuration is equilibrated using a canonical ensemble (NVT) MC simulation.
(3) The equilibrated configuration is used as the initial configuration for GCMC simulation at $\mu \gg \mu_{cav}$.
(4) If the simulation undergoes phase change to the vapor-like state, then the simulation is stopped and bulk chemical potential is recorded as 1 sample in the distribution of cavitation chemical potentials. If the simulation finishes in the liquid state, then μ is decreased by a small amount and a new GCMC simulation is started.
(5) Step 4 is repeated until the simulation reaches a low-density, vapor-like state, the last value of μ is taken as the chemical potential of cavitation μ_{cav}.

Multiple desorption trajectories are calculated independently for a given system, and the distribution of cavitation chemical potential is obtained and analyzed using traditional statistical methods. All simulations used the same number of MC steps so they can be compared to each other; 300 000 MC steps (each step a single attempt to displace or exchange a particle, with equal probability) of 500 equilibrating sets that are discarded, and 500 production sets that are averaged and used as the result. It has been shown that the width of GCMC hysteresis (and thus, the cavitation pressure) is affected by the length of the underlying Markov chain.[58] Therefore, comparisons are only made between average cavitation pressures calculated using equal length GCMC runs.

4. RESULTS AND DISCUSSION

We calculated grand canonical and gauge cell canonical isotherms for LJ nitrogen at 77.36 K adsorbing in a silica pore of diameter 5.54 nm with a single nonwetting heterogeneous defect with diameters ranging from 0 to 2.12 nm. The MC isotherms are displayed in Figure 4. On the vapor branch of the canonical

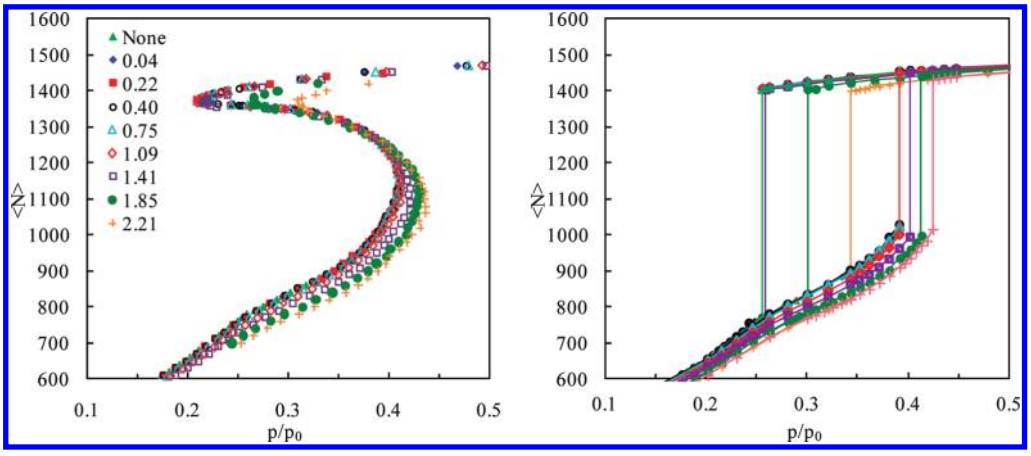

Figure 4. MCMC isotherms (left) and GCMC isotherms (right) for LJ nitrogen adsorbing in a silica pore of 5.54 nm at 77.36 K, with a heterogeneous defect of varying diameter in nm.

dx.doi.org/10.1021/la300078k | *Langmuir* 2012, 28, 4702–4711

isotherms that corresponds to the formation of the adsorbed film, the adsorption depends on the size of the defect. As the defect size increases, the averaged adsorption potential, as well as the surface available for the film formation, decreases, resulting in a lower adsorption relative to the defect-free pore at the same vapor pressure. This trend continues with the position of the vapor spinodal, the maximum chemical potential of the vapor branch that reflects the limit of stability of the adsorbed film. However, the position of the liquid spinodal (the minimum chemical potential of the liquid branch that reflects the limit of stability of the liquid phase) shows two distinct behaviors, depending on the size of the defect. When the defect is less than 1.41 nm, the position of the liquid spinodal increases only slightly with the size of the defect. At larger defects, the spinodal shifts to higher pressures, progressively with the size of the defect. A similar dependence on the defect size is observed on the GCMC isotherms. The condensation pressure increases with defect size, but the cavitation pressure remains mostly unchanged for defects smaller that 1.41 nm. With larger defects, the cavitation pressure increases progressively with the defect size.

To estimate the distribution of cavitation pressure in GCMC simulations, we performed a series of parallel GCMC desorption runs starting from randomly chosen initial configurations equilibrated at a fluid density known a pirori to be a stable liquid. Standard statistical methods where used to obtain the mean cavitation pressure and its dispersion. The cavitation pressures were calculated for the defects of 0, 0.40, 1.41, 1.47, 1.61, 1.85, and 2.21 nm in diameter. Selected distributions from this study are presented in Figure 5.

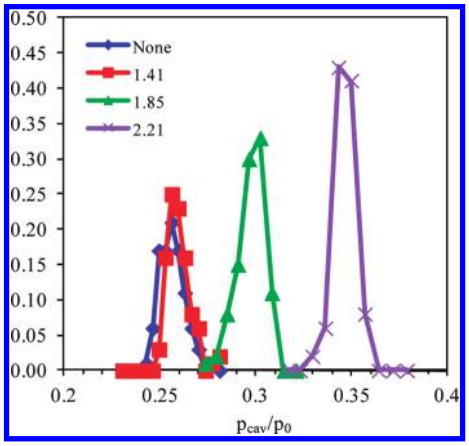

Figure 5. Selected distributions for the pressure of cavitation calculated from a series of independent GCMC desorption paths: pores with no defect (diamond), d_{def} = 1.41 nm (square), 1.85 nm (triangle), and 2.21 nm (cross).

The distributions are bell-shaped. In the pores with larger defects that exhibit predominantly heterogeneous mechanism of cavitation, the distribution of cavitation pressures appears to be narrower than that in the pores with small defects and the homogeneous mechanism of cavitation. The averaged results of these desorption trajectories are displayed in Figure 6. The data can be divided into two regimes of weak and strong dependence on the defect size. From 0 to 1.41 nm diameter of the defect, the average cavitation pressure marginally increases. The increase is small but statistically significant (see Figure 6, inset). For defects larger than 1.41 nm, a strong dependence is observed. It is important to remember that the reported cavitation pressures should not correspond to

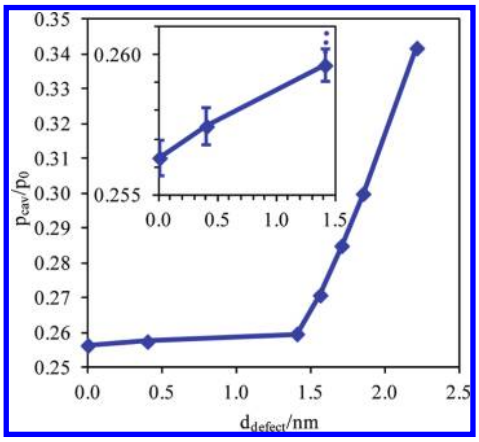

Figure 6. The average pressure of cavitation calculated in a series of independent GCMC simulations. The sharp change of slope indicates the transition from homogeneous to heterogeneous nucleation, determined by examination of particle configurations. Inset zooms on the small defect regime of homogeneous cavitation; error bars represent the standard error of the distribution.

experimental values. The conditions of a MC simulation represent a "perfect" situation of fixed temperature and vapor pressure and with significantly smaller fluctuations than in real experiments. However, *relative* comparisons between calculated GCMC pressures are permissible.

Determination of the type of nucleation was done by tracing the progress of each MC simulation for states near the point of desorption. During the MC simulation, the coordinates of each successful MC move were saved, up to 825 000 moves total. At a specified fluid density (small enough to ensure a phase change occurred; $N\sigma^3/V = 0.4$ for this study), the tracking was stopped and the current configuration written to disk. With this information, the original system (up to 825 000 successful moves ago) can be fully recreated, and examined step-by-step. Figure 7 shows several intermediate states along a desorption path for the pore with none, small (0.40 nm) and large (1.85 nm) defect. The snapshots were created by dividing the available trajectory into 20 frames, and calculating the average particle positions of each frame using 40 equal-spaced samples from the configuration trajectory. Thus, the color intensity indicates the probability of a particle intersecting the *xz*-plane for a given span of simulation time. With configuration snapshots available, formation of the critical nuclei can be observed as fluid particles "desorb" from the pore body. We found that if the defect is larger than 1.41 nm, all nucleation appears to be heterogeneous, that is, the critical nuclei forms at the site of defect and expands from that point, as illustrated in Figure 7. Below this defect size, nucleation is almost always homogeneous; forming at or near the center of the pore. Interestingly, the location of the critical bubble varies on the *xz*-plane more than expected. In pores with a defect, the location of the critical cavity varied from the center of the pore to near the defect (but still entirely within the liquid) to the site of the defect. Even in the no-defect system, the cavity forms near the center, but not always at the center. The relative frequency of each type of cavitation is presented in Figure 8. To compile the statistics of homogeneous and heterogeneous cavitation events from MC runs, trajectories from 30 desorption runs were stored and analyzed. The CNT prediction is also displayed in Figure 8 for comparison. The CNT curve in Figure 8 was obtained with eq 7 by interpolating the cavitation pressure for a given d_{def}, and then calculating the critical bubble radius (eq 2) from that pressure.

dx.doi.org/10.1021/la300078k | *Langmuir* 2012, 28, 4702−4711

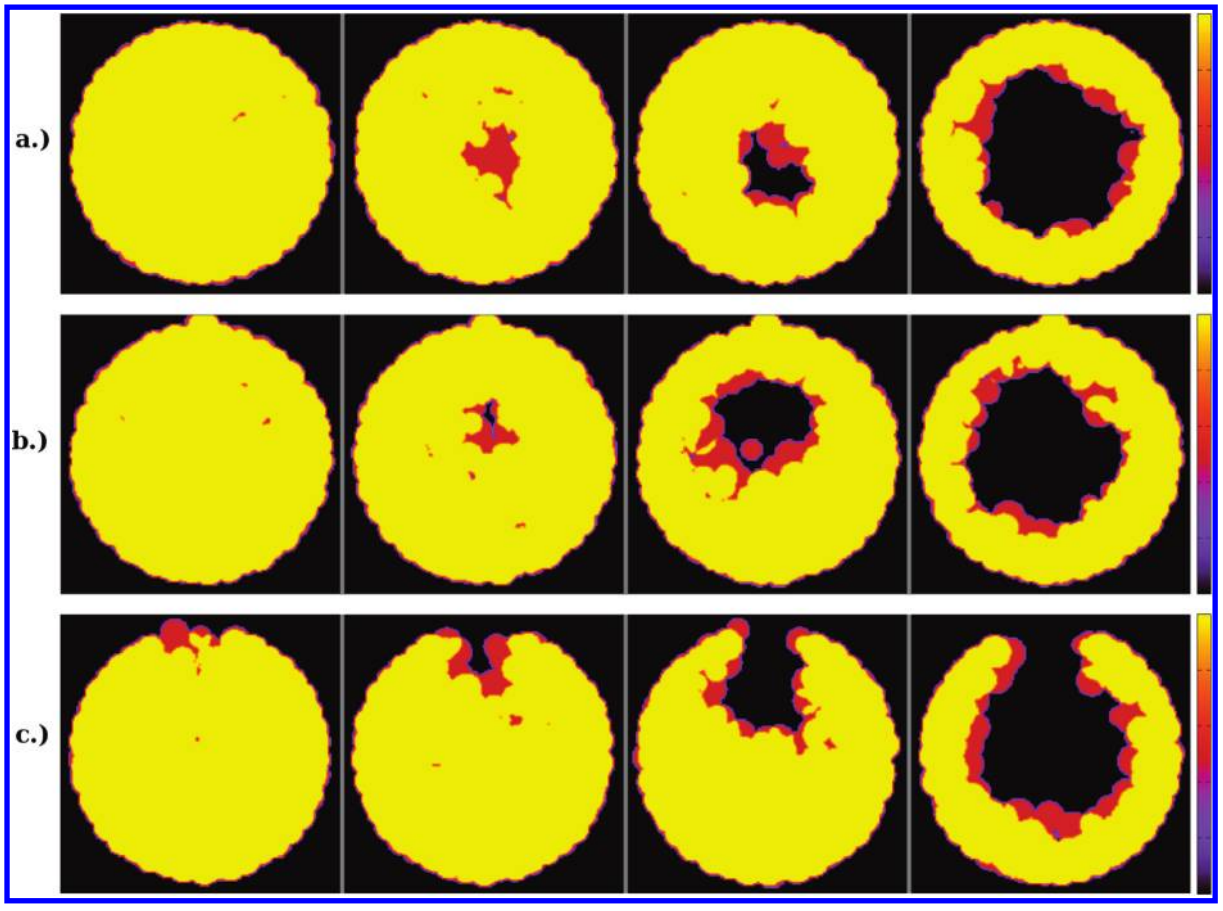

Figure 7. Snapshots of growing bubbles quantified by the particle probabilities on the *xz*-plane during desorption; yellow indicates the probability of unity and black the probability of zero. (a) Pore without defect shows the nucleation of the critical cavity at the center of the pore. (b) Pore with a small defect (0.40 nm) still exhibits homogeneous nucleation. (c) Pore with 1.85 nm defect exhibits a flat interface at complete pore filling, followed by the growth the bubble pinned to the defect; this bubble grows until the vapor-like state is reached.

Instead of using the Kelvin-Laplace relation as above, the equilibrium liquid and vapor pressures were obtained through the JZG equation of state for LJ fluid.[47] The liquid−vapor surface tension ($\gamma\sigma^2/\varepsilon$ = 1.022 for infinite cutoff LJ fluid) was calculated by linear interpolation at T^* = 0.762 from three studies of LJ surface tension,[59−61] and then averaged. The same qualitative shape of the probability curve is obtained using both CNT and MC. CNT predicts the critical defect size to be ∼1.0 nm (∼2.8σ_{FF}, very close the prediction in Figure 2 of ∼3σ), while the MC transition to heterogeneous cavitation takes place at $d_{def} \approx$ 1.5 nm, or about 4σ_{FF}. This quantitative discrepancy between MC and CNT predictions is expected.

Nucleation barriers were calculated via thermodynamic integration of the canonical isotherm from gauge cell calculations to yield the difference in grand thermodynamic potential,

$$\Omega(\mu) - \Omega(\mu_{ref}) = -\int_{\mu_{ref}}^{\mu} N(\mu)d\mu \tag{11}$$

Since cavitation is a nucleation based phenomenon, an energy barrier must be crossed for it to occur. The calculated nucleation barriers are presented in Figure 9. Systems exhibiting homogeneous cavitation (i.e., d_{defect}/nm = 0, 0.40, and 1.41) are found to have nearly identical nucleation barriers. This is expected, as systems with cavitation at similar pressures would be crossing the same energy barrier. When heterogeneous cavitation is found to be the dominant mechanism, the nucleation barrier for a given pressure shifts significantly to lower values. In other words, for a given nucleation barrier, the pressure is found to be constant for homogeneous cavitation, and increasing with defect size for heterogeneous cavitation. Observed cavitations pressures (Figure 6) indicate that the thermal barrier to overcome for GCMC nucleation, regardless

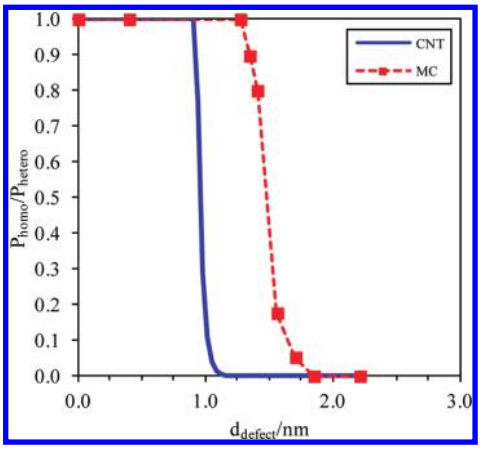

Figure 8. Ratio of the probability of homogeneous nucleation opposed to heterogeneous nucleation. The solid line indicates the prediction from CNT for a system similar to that studied by MC (LJ nitrogen using the JZG equation[47]). The squares are the results from MC simulation trajectories, discussed below.

dx.doi.org/10.1021/la300078k | *Langmuir* 2012, 28, 4702−4711

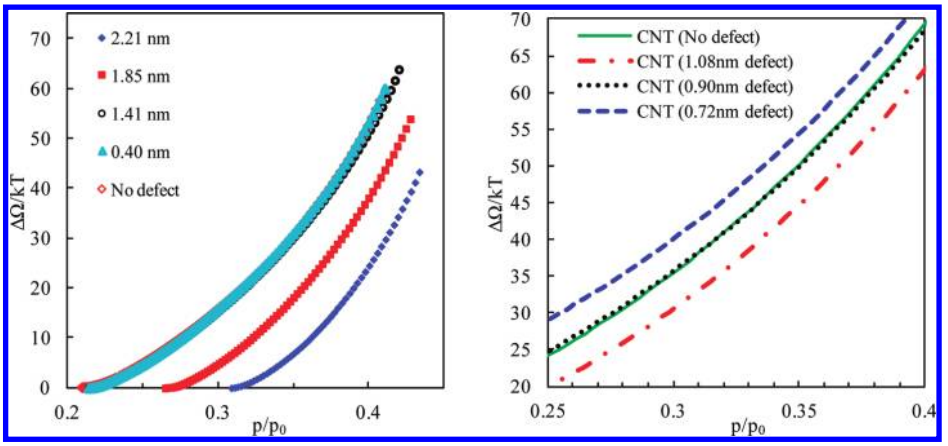

Figure 9. The work of formation of the critical nuclei calculated by thermodynamic integration of the canonical MC isotherms (left) and using the CNT equations for homogeneous and heterogeneous cavitation (right). For comparison of the rates of homogeneous and heterogeneous cavitation, the work of homogeneous cavitation (eq 1) was corrected by the volume factor (eq 6). CNT predicts that the transition to heterogeneous cavitation occurs at a defect d_{def} = 0.90 nm, while MC simulations indicate $d_{def} \approx$ 1.40 nm. Note the large difference in the nucleation barriers calculated with CNT and MC simulations; the reason for this discrepancy is that the size of nuclei in this example does not exceed $d \approx$ 0.90 nm, which is too small for the CNT theory to be quantitatively accurate.

of its nature, is 8−10 k_BT, which is in an acceptable range comparing to literature results.[62] For comparison, results from CNT are included as well on the right-hand side of Figure 9. The CNT curves were calculated using a similar method as described for Figure 8.[63] We see that a defect of d_{def}/nm = 0.90 is the critical size where the predominant nucleation mechanism changes from homogeneous to heterogeneous. The smallest defect (0.72 nm) has a larger barrier than the homogeneous fluid, while the largest defect (1.08 nm) has a smaller barrier, thus dictating the nature of nucleation. The intermediate curve (0.90 nm) is similar in value to the homogeneous curve; at low pressures (small critical bubble), homogeneous nucleation would be more likely, and at higher pressures (larger critical bubble), heterogeneous nucleation would be more likely. As above, the overall transition occurs at a smaller d_{def} than observed in MC simulations, as expected.

5. CONCLUSIONS

We investigated a possible scenario of heterogeneous cavitation of metastable fluid in the process of desorption from mesoporous materials. As a model system, we considered an LJ fluid confined to spherical pores with nonwetting surface defects. We showed that the nonwetting defect facilitates the formation of heterogeneous nuclei, and the probability of heterogeneous cavitation increases with the defect size. As such, the transition from the homogeneous to heterogeneous cavitation occurs in pores with sufficiently large defects. We employed the classical nucleation theory (CNT) and Monte Carlo (MC) simulations to quantify the impact of surface defects on the mechanism of cavitation.

The CNT model was modified to account for heterogeneous nucleation of bubbles at the nonwetting defect. We found that the CNT model describes the transition from the homogeneous to heterogeneous cavitation at sufficiently large surface defects. In such pores, the vapor pressure of cavitation exceeds the vapor pressure characteristic of homogeneous cavitation. The results of the CNT model were examined with the MC simulation study using the mesocanonical ensemble for generating the critical nuclei configurations and determining the nucleation barriers, and the grand canonical ensemble for calculating the distribution of pressures at which cavitation occurs in simulation. The MC results are qualitatively similar to that predicted by CNT and provide a more reliable quantitative estimate of the pressures of cavitation presented in Figure 6. We found that defects smaller than 1.41 nm (or about 5 molecular diameters) do not change the nature of bubble nucleation from the homogeneous case with no defect present. Conversely, surface defects larger than 1.41 nm facilitate competitive heterogeneous nucleation. This leads to a sharp increase in the cavitation pressure with the size of the defect, as the nucleation barrier for forming a heterogeneous bubble pinned to the defect becomes progressively smaller than the nucleation barrier of homogeneous cavitation.

It is worth noting that although the experimental motivation of this work was a series of papers on the mechanism of nitrogen and argon adsorption on porous silicon samples,[2,28,29] our conclusions cannot be applied to this particular system, since it is unlikely that nonwetting (to nitrogen) defects may be present on a silicon surface. At the same time, the scenario of heterogeneous cavitation may be an important factor in adsorption of water and other polar vapors.[64] To consider these systems, it will be necessary to perform a similar simulation study with forcefields adequate for water and water−substrate interaction. Among the other physical processes for which heterogeneous nucleation of bubbles in pores may be an important factor are: drying of porous and fibrous materials,[11] sap breakage in plants,[65] fluid flow in soil and rock,[66] as well as physiological phenomena such as decompression sickness.

AUTHOR INFORMATION

Corresponding Author

*E-mail: aneimark@rutgers.edu.

Present Address

[†]Princeton University, Department of Civil and Environmental Engineering, E228 Engineering Quadrangle, Princeton, New Jersey, 08544, U.S.A.

Notes

The authors declare no competing financial interest.

ACKNOWLEDGMENTS

This work was supported by the NSF IGERT in Nanopharmaceutical Engineering, the Venkatarama Fellowship awarded

to C.J.R. and by the NSF Engineering Research Center for Structured Organic Particulate Systems (ERC-SOPS).

REFERENCES

(1) Reichenbach, C.; Kalies, G.; Enke, D.; Klank, D. Cavitation and Pore Blocking in Nanoporous Glasses. *Langmuir* **2011**, *27* (17), 10699−10704.
(2) Grosman, A.; Ortega, C. Cavitation in Metastable Fluids Confined to Linear Mesopores. *Langmuir* **2011**, *27* (6), 2364−2374.
(3) Fan, C.; Do, D. D.; Nicholson, D. On the Cavitation and Pore Blocking in Slit-Shaped Ink-Bottle Pores. *Langmuir* **2011**, *27* (7), 3511−3526.
(4) Rasmussen, C. J.; Vishnyakov, A.; Thommes, M.; Smarsly, B. M.; Kleitz, F.; Neimark, A. V. Cavitation in Metastable Liquid Nitrogen Confined to Nanoscale Pores. *Langmuir* **2010**, *26* (12), 10147−10157.
(5) Ravikovitch, P. I.; Neimark, A. V. Experimental Confirmation of Different Mechanisms of Evaporation from Ink-Bottle Type Pores: Equilibrium, Pore Blocking, and Cavitation. *Langmuir* **2002**, *18* (25), 9830−9837.
(6) Thommes, M.; Smarsly, B.; Groenewolt, M.; Ravikovitch, P. I.; Neimark, A. V. Adsorption Hysteresis of Nitrogen and Argon in Pore Networks and Characterization of Novel Micro- and Mesoporous Silicas. *Langmuir* **2006**, *22* (2), 756−764.
(7) Monson, P. A. Fluids Confined in Porous Materials: Towards a Unified Understanding of Thermodynamics and Dynamics. *Chemie Ingenieur Technik* **2011**, *83* (1−2), 143−151.
(8) Nguyen, P. T. M.; Do, D. D.; Nicholson, D. On The Cavitation and Pore Blocking in Cylindrical Pores with Simple Connectivity. *J. Phys. Chem. B* **2011**, *115* (42), 12160−12172.
(9) Morishige, K.; Tateishi, M.; Hirose, F.; Aramaki, K. Change in Desorption Mechanism from Pore Blocking to Cavitation with Temperature for Nitrogen in Ordered Silica with Cagelike Pores. *Langmuir* **2006**, *22* (22), 9220−9224.
(10) Sarkar, A.; Chaudhuri, S. R.; Wang, S.; Kirkbir, F.; Murata, H. Drying of Alkoxide Gels−Observation of an Alternate Phenomenology. *J. Sol-Gel Sci. Technol.* **1994**, *2* (1−3), 865−870.
(11) Scherer, G. W.; Smith, D. M. Cavitation during Drying of a Gel. *J. Non-Cryst. Solids* **1995**, *189* (3), 197−211.
(12) Parlar, M.; Yortsos, Y. C. Nucleation and Pore Geometry Effects in Capillary Desorption Processes in Porous Media. *J. Colloid Interface Sci.* **1989**, *132* (2), 425−443.
(13) Parlar, M.; Yortsos, Y. C. Percolation Theory of Vapor Adsorption—Desorption Processes in Porous Materials. *J. Colloid Interface Sci.* **1988**, *124* (1), 162−176.
(14) Esparza, J. M.; Ojeda, M. L.; Campero, A.; Hernández, G.; Felipe, C.; Asomoza, M.; Cordero, S.; Kornhauser, I.; Rojas, F. Development and Sorption Characterization of Some Model Mesoporous and Microporous Silica Adsorbents. *J. Mol. Catal A: Chem.* **2005**, *228* (1−2), 97−110.
(15) Gobin, O. C.; Wan, Y.; Zhao, D.; Kleitz, F.; Kaliaguine, S. Mesostructured Silica SBA-16 with Tailored Intrawall Porosity Part 1: Synthesis and Characterization. *J. Phys. Chem. C* **2007**, *111* (7), 3053−3058.
(16) Haffer, S.; Tiemann, M.; Fröba, M. Periodic Mesoporous Organosilica (PMO) Materials with Uniform Spherical Core-Shell Structure. *Chem.—Eur. J.* **2010**, *16*, 10447−10452.
(17) Kleitz, F.; Czuryszkiewicz, T.; Solovyov, L. A.; Linden, M. X-ray Structural Modeling and Gas Adsorption Analysis of Cagelike SBA-16 Silica Mesophases Prepared in a F127/Butanol/H_2O System. *Chem. Mater.* **2006**, *18* (21), 5070−5079.
(18) Morishige, K.; Ishino, M. Lower Closure Point of Adsorption Hysteresis in Ordered Mesoporous Silicas. *Langmuir* **2007**, *23* (22), 11021−11026.
(19) Neimark, A. V.; Vishnyakov, A. The Birth of a Bubble: A Molecular Simulation Study. *J. Chem. Phys.* **2005**, *122* (5), 054707.
(20) Vishnyakov, A.; Neimark, A. V. Monte Carlo Simulation Test of Pore Blocking Effects. *Langmuir* **2003**, *19* (8), 3240−3247.
(21) Woo, H.-J.; Porcheron, F.; Monson, P. A. Modeling Desorption of Fluids from Disordered Mesoporous Materials. *Langmuir* **2004**, *20* (11), 4743−4747.
(22) Coasne, B.; Gubbins, K. E.; Pellenq, R. J. M. A Grand Canonical Monte Carlo Study of Adsorption and Capillary Phenomena in Nanopores of Various Morphologies and Topologies: Testing the BET and BJH Characterization Methods. *Part. Part. Syst. Charact.* **2004**, *21*, 149−160.
(23) Libby, B.; Monson, P. A. Adsorption/Desorption Hysteresis in Inkbottle Pores: A Density Functional Theory and Monte Carlo Simulation Study. *Langmuir* **2004**, *20* (10), 4289−4294.
(24) Sarkisov, L.; Monson, P. A. Hysteresis in Monte Carlo and Molecular Dynamics Simulations of Adsorption in Porous Materials. *Langmuir* **2000**, *16* (25), 9857−9860.
(25) Sarkisov, L.; Monson, P. A. Modeling of Adsorption and Desorption in Pores of Simple Geometry Using Molecular Dynamics. *Langmuir* **2001**, *17* (24), 7600−7604.
(26) Zhao, D.; Feng, J.; Huo, Q.; Melosh, N.; Fredrickson, G. H.; Chmelka, B. F.; Stucky, G. D. Triblock Copolymer Syntheses of Mesoporous Silica with Periodic 50 to 300 Angstrom Pores. *Science* **1998**, *279* (5350), 548.
(27) Coasne, B.; Galarneau, A.; Di Renzo, F.; Pellenq, R. J. M. Effect of Morphological Defects on Gas Adsorption in Nanoporous Silicas. *J. Phys. Chem. C* **2007**, *111* (43), 15759−15770.
(28) Naumov, S.; Khokhlov, A.; Valiullin, R.; Kärger, J.; Monson, P. A. Understanding Capillary Condensation and Hysteresis in Porous Silicon: Network Effects within Independent Pores. *Phys. Rev. E* **2008**, *78* (6), 060601.
(29) Wallacher, D.; Künzner, N.; Kovalev, D.; Knorr, N.; Knorr, K. Capillary Condensation in Linear Mesopores of Different Shape. *Phys. Rev. Lett.* **2004**, *92* (19), 195704.
(30) Coasne, B.; Grosman, A.; Ortega, C.; Simon, M. Adsorption in Noninterconnected Pores Open at One or at Both Ends: A Reconsideration of the Origin of the Hysteresis Phenomenon. *Phys. Rev. Lett.* **2002**, *88* (25), 256102.
(31) Ravikovitch, P. I.; Neimark, A. V. Characterization of Nanoporous Materials from Adsorption and Desorption Isotherms. *Colloids Surf., A* **2001**, *187−188*, 11−21.
(32) Gregg, S. J.; Sing, K. S. W. *Adsorption, Surface Area and Porosity*; Academic Press: New York, 1982.
(33) Rouquerol, F.; Rouquerol, J.; Sing, K. S. W. *Adsorption by Powders and Porous Solids: Methodology and Applications*; Academic Press: San Diego, CA, 1999.
(34) Naumov, S.; Valiullin, R.; Kärger, J.; Monson, P. A. Understanding Adsorption and Desorption Processes in Mesoporous Materials with Independent Disordered Channels. *Phys. Rev. E* **2009**, *80* (3), 031607.
(35) Kumar, P.; Hofmann, T.; Knorr, K.; Huber, P.; Scheib, P.; Lemmens, P. Tuning the Pore Wall Morphology of Mesoporous Silicon from Branchy to Smooth, Tubular by Chemical Treatment. *J. Appl. Phys.* **2008**, *103* (2), 024303.
(36) Neimark, A. V.; Ravikovitch, P. I.; Grün, M.; Schüth, F.; Unger, K. K. Pore Size Analysis of MCM-41 Type Adsorbents by Means of Nitrogen and Argon Adsorption. *J. Colloid Interface Sci.* **1998**, *207* (1), 159−169.
(37) Ravikovitch, P. I.; Wei, D.; Chueh, W. T.; Haller, G. L.; Neimark, A. V. Evaluation of Pore Structure Parameters of MCM-41 Catalyst Supports and Catalysts by Means of Nitrogen and Argon Adsorption. *J. Phys. Chem. B* **1997**, *101* (19), 3671−3679.
(38) Debenedetti, P. G. *Metastable Liquids*; Princeton University Press: Princeton, NJ, 1996.
(39) Frenkel, J. I., *Kinetic Theory of Liquids*; Oxford University Press: London, 1946.
(40) Ford, I. J. Statistical Mechanics of Nucleation: A Review. *Proc. Inst. Mech. Eng. Part C-J. Eng. Mech. Eng. Sci.* **2004**, *218* (8), 883−899.
(41) Tolman, R. C. The Effect of Droplet Size on Surface Tension. *J. Chem. Phys.* **1949**, *17* (3), 333−337.
(42) The volume of each bubble corresponds to the difference in volumes of intersecting spherical caps, one cap being the bubble, a

sphere of radius r_b and second the pore, a sphere of radius R. The height of the cap is governed by the whether the bubble is the small or large configuration, and the size of the defect, r_{def}. The volume of the stable (smaller) bubble is $V_s = \pi/3\ [R^3(\cos^3\alpha - 3\cos\alpha + 2) + r_b^3(\cos^3\beta - 3\cos\beta + 2)]$ and the larger, unstable bubble is $V_u = \pi/3\ [R^3(\cos^3\alpha - 3\cos\alpha + 2) - r_b^3(\cos^3\beta - 3\cos\beta - 2)]$, where α and β are $\alpha = \arcsin(r_{def}/R)$ and $\beta = \arcsin(r_{def}/r_b)$. Similarly, the surface areas of the stable and unstable bubble are $S_s = 2\pi r_b^2(1 - \cos\beta)$ and $S_u = 2\pi r_b^2(1 + \cos\beta)$, respectively.

(43) Do, D. D.; Do, H. D. Appropriate volumes for adsorption isotherm studies: The absolute void volume, accessible pore volume and enclosing particle volume. *J. Colloid Interface Sci.* **2007**, *316* (2), 317−330.

(44) Ravikovitch, P. I.; Vishnyakov, A.; Russo, R.; Neimark, A. V. Unified Approach to Pore Size Characterization of Microporous Carbonaceous Materials from N_2, Ar, and CO_2 adsorption isotherms. *Langmuir* **2000**, *16* (5), 2311−2320.

(45) Baksh, M. S. A.; Yang, R. T. Model For Spherical Cavity Radii And Potential Functions Of Sorbates In Zeolites. *AIChE J.* **1991**, *37* (6), 923−930.

(46) Ravikovitch, P. I.; Neimark, A. V. Density Functional Theory of Adsorption in Spherical Cavities and Pore Size Characterization of Templated Nanoporous Silicas with Cubic and Three-Dimensional Hexagonal Structures. *Langmuir* **2002**, *18* (5), 1550−1560.

(47) Johnson, J. K.; Zollweg, J. A.; Gubbins, K. E. The Lennard−Jones equation of state revisited. *Mol. Phys.* **1993**, *78* (3), 591−618.

(48) Goldman, R. *Rethinking Quaternions: Theory and Computation*; Morgan & Claypool Publishers: 2010.

(49) Norman, G. E.; Filinov, V. S. Investigation of Phase Transitions by the Monte Carlo Method. *High Temp. (USSR)* **1969**, *7*, 216−222.

(50) Neimark, A. V.; Vishnyakov, A. Gauge Cell Method for Simulation Studies of Phase Transitions in Confined Systems. *Phys. Rev. E* **2000**, *62* (4), 4611.

(51) Neimark, A. V.; Vishnyakov, A. a Simulation Method for the Calculation of Chemical Potentials in Small, Inhomogeneous, And Dense Systems. *J. Chem. Phys.* **2005**, *122* (23), 234108−11.

(52) Vishnyakov, A.; Neimark, A. V. Multicomponent Gauge Cell Method. *J. Chem. Phys.* **2009**, *130* (22), 224103−9.

(53) Rasmussen, C. J.; Vishnyakov, A.; Neimark, A. V. Monte Carlo Simulation of Polymer Adsorption. *Adsorption* **2011**, *17* (1), 265−271.

(54) Rasmussen, C. J.; Vishnyakov, A.; Neimark, A. V. Calculation of Chemical Potentials of Chain Molecules by the Incremental Gauge Cell Method. *J. Chem. Phys.* **2011**, *135* (21), 214109.

(55) Neimark, A. V.; Vishnyakov, A. Vapor-to-Droplet Transition in a Lennard−Jones Fluid: Simulation Study of Nucleation Barriers Using the Ghost Field Method. *J. Phys. Chem. B* **2005**, *109* (12), 5962−5976.

(56) Neimark, A. V.; Vishnyakov, A. Monte Carlo Simulation Study of Droplet Nucleation. *J. Chem. Phys.* **2005**, *122* (17), 174508−11.

(57) Haahr, M. Random.org: True Random Number Service. http://www.random.org

(58) Schoen, M.; Rhykerd, C. L.; Cushman, J. H.; Diestler, D. J. Slit-Pore Sorption Isotherms by the Grand-Canonical Monte Carlo Method. *Mol. Phys.* **1989**, *66* (6), 1171−1182.

(59) Errington, J. R. Evaluating Surface Tension Using Grand-Canonical Transition-Matrix Monte Carlo Simulation and Finite-Size Scaling. *Phys. Rev. E* **2003**, *67* (1), 012102.

(60) Chen, B.; Siepmann, J. I.; Oh, K. J.; Klein, M. L. Aggregation-Volume-Bias Monte Carlo Simulations of Vapor-Liquid Nucleation Barriers for Lennard−Jonesium. *J. Chem. Phys.* **2001**, *115* (23), 10903−10913.

(61) Mecke, M.; Winkelmann, J.; Fischer, J. Molecular Dynamics Simulation of the Liquid−Vapor Interface: The Lennard−Jones Fluid. *J. Chem. Phys.* **1997**, *107* (21), 9264−9270.

(62) Punnathanam, S.; Corti, D. S. Homogeneous Bubble Nucleation in Stretched Fluids: Cavity Formation in the Superheated Lennard−Jones Liquid. *Ind. Eng. Chem. Res.* **2002**, *41* (5), 1113−1121.

(63) It is worth noting that the numerical results of CNT and GCMC calculations for no defect pores differ somewhat from the data in our previous paper because of the different value of the LJ potential cutoff of 10σ instead 5σ. This also affected the CNT calculations by altering the equation of state and the surface tension value (1.022 vs 0.922).

(64) Luzar, A.; Leung, K. Dynamics of Capillary Evaporation. I. Effect of Morphology of Hydrophobic Surfaces. *J. Chem. Phys.* **2000**, *113* (14), 5836−5844.

(65) Cochard, H. Cavitation in Trees. *C. R. Physique* **2006**, *7*, 1018−1026.

(66) Or, D.; Tuller, M. Cavitation during Desaturation of Porous Media under Tension. *Water Resour. Res.* **2002**, *38* (5), 1061.